Molecular Mechanism of ATP Hydrolysis in F$_1$-ATPase Revealed by Molecular Simulations and Single-Molecule Observations

Shigehiko Hayashi,*,[†] Hiroshi Ueno,[‡] Abdul Rajjak Shaikh,[†] Myco Umemura,[†] Motoshi Kamiya,[†] Yuko Ito,[§] Mitsunori Ikeguchi,[§] Yoshihito Komoriya,[‖] Ryota Iino,[⊥] and Hiroyuki Noji[⊥]

[†]Department of Chemistry, Graduate School of Science, Kyoto University, Kyoto 606-8502, Japan

[‡]Department of Physics, Faculty of Science and Engineering, Chuo University, Bunkyo-ku, Tokyo 112-8551, Japan
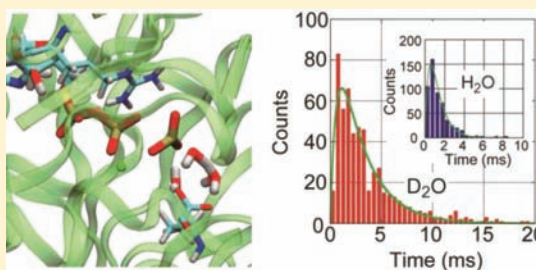
[§]Department of Supramolecular Biology, Graduate School of Nanobioscience, Yokohama City University, Tsurumi-ku, Yokohama 230-0045, Japan

[‖]Institute of Scientific and Industrial Research, Osaka University, Ibaraki, Osaka 567-0047, Japan

[⊥]Department of Applied Chemistry, School of Engineering, The University of Tokyo, Bunkyo-ku, Tokyo 113-8656, Japan

Ⓢ *Supporting Information*

ABSTRACT: Enzymatic hydrolysis of nucleotide triphosphate (NTP) plays a pivotal role in protein functions. In spite of its biological significance, however, the chemistry of the hydrolysis catalysis remains obscure because of the complex nature of the reaction. Here we report a study of the molecular mechanism of hydrolysis of adenosine triphosphate (ATP) in F$_1$-ATPase, an ATP-driven rotary motor protein. Molecular simulations predicted and single-molecule observation experiments verified that the rate-determining step (RDS) is proton transfer (PT) from the lytic water molecule, which is strongly activated by a metaphosphate generated by a preceding P$_\gamma$–O$_\beta$ bond dissociation (POD). Catalysis of the POD that triggers the chain activation of the PT is fulfilled by hydrogen bonds between Walker motif A and an arginine finger, which commonly exist in many NTPases. The reaction mechanism unveiled here indicates that the protein can regulate the enzymatic activity for the function in both the POD and PT steps despite the fact that the RDS is the PT step.

■ INTRODUCTION

Hydrolysis of triphosphate bound to a nucleotide [nucleotide triphosphate (NTP)] is one of the most fundamental reactions in protein functions. The hydrolysis of a high-energy substrate NTP into a nucleotide diphosphate (NDP) and an inorganic phosphate (P$_i$) generates ~45 kJ/mol of energy, which is used in various proteins such as motor,[1−4] transporter,[5] and signaling[6] proteins. The extremely high catalytic activity of the NTPase enzymes (reaching 10^9-fold) enables the proteins to make use of the energy stored in the triphosphate for their functions.

Despite its biological importance, however, the chemical mechanisms of the catalytic activity and even the hydrolysis reaction itself remain obscure for any one of the NTPases. Experimentally, kinetic measurements with mutants that alter the catalytic rate constant (k_{cat}) provide insights into the reaction mechanism. However, in principle, k_{cat} can include not only the hydrolysis reaction rate but also rate components associated with other events in the overall enzymatic process such as ligand unbinding and protein conformational changes.[7] Furthermore, the perturbation introduced by the mutations can lead to large protein structural disorder from the native structure. These ambiguities obstruct clear interpretation of the kinetic observations.

On the other hand, theoretical approaches such as the hybrid quantum-mechanical/molecular-mechanical (QM/MM) methodology enable one to examine in atomic detail the chemical reaction profile in the protein environment.[8−17] However, the reaction mechanisms proposed to date are diverse, even for the same protein, depending on the simulation protocols and computational accuracies. Because of the difficulty of providing a quantum-chemical description of the highly polar electronic nature of the triphosphate substrate and the binding pocket, theoretical modeling would require solid verification based on experimental evidence.

In the present study, we investigated the reaction mechanism of adenosine triphosphate (ATP) hydrolysis in the motor protein F$_1$-ATPase[2−4,18−20] by a combination of molecular simulations and single-molecule observation experiments. Using the energy of the ATP hydrolysis reactions that occur in the $\alpha_3\beta_3$ subcomplex, the protein rotates the γ subunit, which can be detected by single-molecule observation techniques[21−25] (Figure 1).

F$_1$-ATPase provides a unique opportunity to examine the ATP hydrolysis reaction. Single-molecule observations of the rotation of the γ subunit allow one to distinguish the
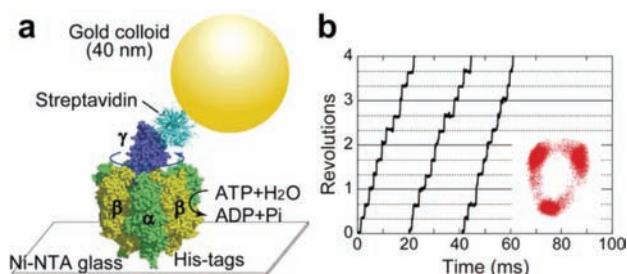
Figure 1. (a) Schematic view of the single-molecule observation of the motor function of F$_1$-ATPase. The $\alpha_3\beta_3$ subcomplex is mounted on a Ni-NTA cover glass with His tags. The rotation of the γ subunit, which is inserted in the center of the $\alpha_3\beta_3$ ring, upon ATP hydrolysis drives the rotational motion of a gold colloid or magnetic bead attached to the γ subunit through a streptavidin, which is observed by objective-type total internal reflection dark-field microscopy or phase-contrast microscopy (see the Supporting Information). (b) Typical time course and (inset) a trace of the rotational motion. At high ATP concentration, one revolution is observed to comprise three discrete 120° steps, each of which consumes one ATP. Each dwell between the steps involves an ATP hydrolysis reaction and release of a P$_i$. Analysis of the dwelling time determines the reaction rate of ATP hydrolysis.

elementary step of the ATP hydrolysis reaction from other events in the enzymatic process.[22,26−29] This advantage, together with an improved time resolution of the single-molecule observations developed in the present study,[30] made it possible to determine the kinetic rates exclusively relevant to the hydrolysis reactions.

The reaction profile was first examined by ab initio QM/MM calculations along with careful system preparations using molecular dynamics (MD) simulations. The characteristic reaction mechanism predicted theoretically, which identified the molecular origins of the extremely high catalytic activity, was then verified by single-molecule experiments designed on the basis of the reaction profile. The revealed reaction scheme provides insights into the molecular mechanism of the catalytic activity control requisite for the motor function of F$_1$-ATPase as well as that for the functions of other NTPases with common sequential and structural motifs at the NTP binding sites.

METHODS

MD Simulations. The molecular simulation system was first prepared by MD simulations. The initial structure for the study of ATP hydrolysis in the binding pocket of the β_{DP} subunit was based on an X-ray crystallographic structure determined by Bowler et al.[31] (PDB entry 2JDI). Recent single-molecule experiments[32,33] confirmed that the crystallographic complex structure is trapped in the catalytic dwell state. Hence, the binding pocket of β_{DP} is responsible for the catalytically active reaction site. Although other ATP binding sites in the α and β subunits exhibit distinct sequential and conformational differences, the effects of the differences on the reaction mechanism and the catalytic activity are beyond the scope of the present study. The $\alpha_3\beta_3\gamma$ protein complex structure including crystalline water molecules was solvated in a water box, and Na$^+$ and Cl$^-$ ions at a concentration of 150 mM were added. The total number of atoms was 337 300. All of the MD simulations were carried out with the program MARBLE[34] using force-field parameters of CHARMM22/CMAP for the protein and TIP3P for water molecules. Vacant cavities around the γ-phosphate of ATP observed in the X-ray crystallographic structure were filled with two additional water molecules. The

initial structure for the QM/MM calculations was obtained from a simulated-annealing simulation starting from the final structure of the equilibrium MD trajectory that maintained stable hydrogen-bond network including water molecules around the triphosphate throughout the equilibrium trajectory for 3 ns (see the Supporting Information for details). The binding pocket conformation obtained is in good agreement with that observed in the X-ray crystallographic structure. Details of the construction of the protein structure, including the αArg373Lys mutant and the MD simulation protocols, are described in the Supporting Information.

QM/MM Calculations. A QM/MM system was constructed from the solvated protein system determined by the simulated annealing of the MD trajectory calculation described above. The QM/MM system included residues within 19.9 Å of the QM region, which consisted of the triphosphate part of ATP, a Mg atom, and polar groups surrounding the reactive moieties, specifically, the side chains of αArg373, βLys162, βGlu188, and βArg189 and seven water molecules. QM/MM boundaries at covalent bonds were capped by hydrogen atoms. The total numbers of QM and MM atoms were 86 and 7156, respectively. The reaction path calculations were carried out using a QM/MM method developed previously[35] and implemented in the GAMESS program package.[36] Density functional theory (DFT) with the B3LYP functional and the 6-31G** basis set with diffuse functions for anionic atoms was used for the QM description. Second-order Møller−Plesset single-point calculations were also carried out to assess the quality of the DFT/B3LYP description (see the Supporting Information and Table S1). The MM region was described with the Amber99 force field. The geometries of the QM/MM system were optimized throughout the reaction path. For zero-point energy (ZPE) evaluation, vibrational frequencies of the QM region were calculated with Hessian matrices obtained by finite differences with analytical gradients. QM/MM MD simulations to verify the intrinsic thermal stability of the QM/MM system and to evaluate free energy reaction profiles were shown to be not appropriately applicable for the present system because of either highly demanding computational cost at higher levels of theory for a sufficiently long MD simulation or too-poor accuracy of lower-level methodologies for these purposes (see the Supporting Information for details). Nevertheless, the agreement between the binding pocket conformation obtained from the molecular simulations and that observed in the X-ray crystallographic structure indicates a high stability of the conformation. Furthermore, as described below, the present analysis of the reaction scheme is expected to be less affected by thermal fluctuations. Details of the QM/MM system, including the αArg373Lys mutant and computational protocols, are described in the Supporting Information.

Single-Molecule Observations. The thermophilic F$_1$-ATPase was purified and biotinylated at cysteines of the γ subunit as reported previously. A streptavidin-coated gold colloid (40 nm diameter) was prepared as described previously.[30] The rotation of the γ subunit of F$_1$-ATPase was visualized by attaching a gold colloid to the γ subunit and immobilizing the $\alpha_3\beta_3$ ring on a Ni-NTA-coated cover glass with His tags. The rotation assay mixtures contained 50 mM KCl, 2 mM MgCl$_2$, ATP regenerating system (1 mM creatine phosphate, 0.1 mg/mL creatine kinase), 5 mg/mL BSA, the indicated amount of ATP, and 10 mM 3-(N-morpholino)-propanesulfonic acid (MOPS)/KOH(D) (pH 7.5 and pD 7.5 for the H$_2$O and D$_2$O assay mixtures, respectively). When

indicated, ATPγS was added instead of ATP, and the ATP regenerating system was omitted in this case. Images were obtained by objective-type total internal reflection dark-field microscopy[30] with an inverted optical microscope (IX-71, Olympus) and recorded with a high-speed CMOS camera (FASTCAM-1024PCI, Photron) at 10 000 frames/s. ImageJ (NIH) and custom-made plug-ins (K. Adachi, Gakushuin University) were used to determine the centroid of each particle and the rotary angles from the recorded images. For the αArg364Lys mutant, which corresponds to the αArg373Lys mutant of bovine mitochondrial F_1-ATPase, the rotation of the γ subunit was probed using a magnetic bead (0.2−0.5 μm) at a recording rate of 250 frames/s with an ATP concentration of 1 mM. Details of the experimental setup are described in the Supporting Information.

■ RESULTS

Hydrolysis Reaction Profile Proposed by Molecular Simulations. Figure 2a shows the energy diagram for the
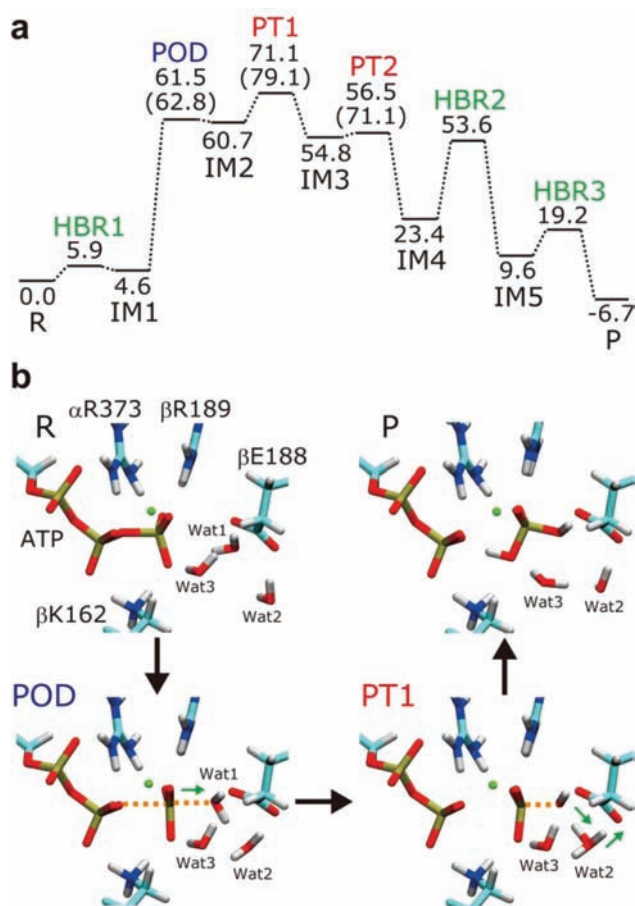

Figure 2. Reaction profile determined by the QM/MM calculations. (a) Energy diagram of the overall reaction path from reactant (R) to product (P). The activation energies for the POD, PT1, and PT2 steps in the TS region include ZPE corrections; the values in parentheses for those steps are the activation energies without the corrections. Energies for the other states do not include ZPE corrections. (b) Structural changes at important states along the reaction path. Green spheres represent the Mg atom. Three water molecules (Wat1−3) in the vicinity of the γ-phosphate and βGlu188, which are directly involved in the reaction process, are shown. The structures of all of the states in the reaction are summarized in the Supporting Information.

overall reaction process determined from the QM/MM calculations. The reaction is composed of bond rearrangement at the γ-phosphate, including $P_γ−O_β$ bond dissociation (POD) and proton transfers (PTs) in the transition state (TS) region, and hydrogen-bond rearrangements (HBRs) of water molecules in the binding pocket, with relatively low activation barriers taking place before and after the TS region.

Figure 2b depicts atomic details of the reaction in the TS region (see the Supporting Information for molecular structures of all of the TSs and intermediate states in the overall reaction process). After HBR from the reactant state, which is requisite for the efficient reaction process in the TS region (see the Supporting Information), the terminal $P_γO_3^-$ moiety is detached by POD from ADP through a pentacovalent TS with an activation energy of 61.5 kJ/mol. Next, a high-energy quasi-stable intermediate state (IM2, 60.7 kJ/mol) is formed in a shallow energy well. In the IM2 state, the metaphosphate-like $P_γO_3^-$ moiety is almost completely dissociated from ADP ($P_γ−O_β$ distance = 2.68 Å; Figure S10 in the Supporting Information). On the other hand, a vacant orbital of $P_γO_3^-$ generated by the dissociation interacts with a lone pair of the lytic water molecule (Wat1), stabilizing the metaphosphate-like conformation.

After the formation of IM2, the lytic water molecule undergoes proton release accompanying the complete formation of the $P_γ−O_w$ bond (Figure 2b and Figure S11 in the Supporting Information). The $P_γ−O_w$ bond length decreases to 1.71 Å upon proton release. A nearby water molecule (Wat2) accepts the proton and then releases the other proton to a carboxyl group of βGlu188, leading to the formation of a high-energy quasi-stable intermediate state (IM3, 54.8 kJ/mol). The relaying water molecule (Wat2) forms a hydronium ion (H_3O^+) at TS PT1 with an activation energy of 71.1 kJ/mol.

The proton at βGlu188 in the IM3 state is transferred to the γ-phosphate via two water molecules (Wat2 and Wat3), and the product state is then formed through HBRs (see Figures S12−S14 in the Supporting Information). The product conformation was confirmed to be stable in thermal equilibrium by means of an MD simulation with ADP and P_i at 300 K (see the Supporting Information and Figure S15). The overall reaction is calculated to be slightly exothermic by −6.7 kJ/mol, which is consistent with recent experimental evidence[29] that the equilibrium constant of the hydrolysis reaction in the protein is 2.9. The small reaction energy indicates that the hydrolysis reaction in the catalytic dwell state does not generate a large amount of energy that can be utilized for the motor function. This view is consistent with an experimental proposal from a single-molecule experiment[37] that generation of the force for the rotation of the γ-subunit is driven mainly by ATP binding and that energy generated by ATP hydrolysis is utilized to rectify thermal equilibrium among the ligand binding and unbinding states.

Sensitivities of the Reaction Rate to the Use of D_2O as the Solvent and the ATPγS Analogue or the αArg373Lys Mutant as the Substrate. As shown in the Discussion, the reaction profile obtained from the calculations was verified by experimental single-molecule measurements of the reaction rates in D_2O solvent and with an analogue substrate, ATPγS, for the native and αArg373Lys mutant[38] proteins. The sensitivities of the reaction rate to the use of D_2O and ATPγS were first examined by QM/MM calculations. Table 1 summarizes rate reduction ratios (RRRs) of the reaction rate in D_2O and for ATPγS. Normal mode analysis predicted that the

Table 1. Activation Energies ($\Delta E^{\ddagger}$) and Rate Reduction Ratios (RRRs) of the Hydrolysis Reactions Evaluated Using QM/MM Simulations

| | Activation Energies and H_2O/D_2O RRRs | | |
| | $\Delta E^{\ddagger}$ (kJ/mol)^a | | |
substrate	H_2O	D_2O	H_2O/D_2O RRR^b
ATP	71.1 (56.1, 54.0^c)	73.6 (58.6)	2.5 (3.0, 6.8^c)
ATPγS	78.7 (64.4)	80.8 (67.4)	2.4 (3.0)
αArg373Lys	88.7 (73.2)	88.7 (72.8)	1.0 (0.88)
	Substrate and Mutant RRRs		
solvent	ATP/ATPγS RRR^b	native/αArg373Lys RRR^b	
H_2O	15 (30, 68^c)	1.1×10^3 (9.1×10^2, 2.1×10^3 ^{c})	
D_2O	18 (31)	4.0×10^2 (2.6×10^2)	

^{a}ZPE-corrected QM/MM activation energies. Values in parentheses are the experimental activation free energies $\Delta G^{\ddagger}$ estimated using the transition-state theory formula $\Delta G^{\ddagger} = -k_B T \ln(h/k_B T\tau)$, where k_B is Boltzmann's constant, T is the absolute temperature (set at 300 K), h is Planck's constant, and τ is the observed time constant corresponding to the hydrolysis reaction (see the text), unless otherwise noted. ^{b}Evaluated as RRR = $\exp(-\Delta\Delta E^{\ddagger}/k_B T)$, where $\Delta\Delta E^{\ddagger}$ is the difference in the activation energies. ^{c}Evaluated using the experimentally observed time constant of 0.4 ms for the native substrate in H_2O.

reaction in D_2O should be almost 3 times slower than that in H_2O (RRR = 2.5). Activation energy calculations for ATPγS (see the Supporting Information) also demonstrated that using ATPγS as the substrate should decrease the rate by a factor of 15. Hence, the QM/MM calculations indicate that the reaction rate is sensitive to the use of both D_2O and ATPγS.

The hydrolysis reaction rates in D_2O as the solvent and for ATPγS as the substrate were then measured by a single-molecule observation technique. The catalytic dwell for a pause between one-step rotations of 120° (Figure 1b) involves two processes, suggested to be the hydrolysis reaction and a P_i release.[28,29,39] Figure 3 shows histograms of the dwelling time
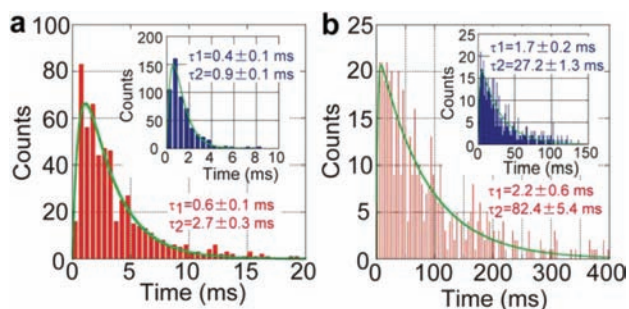

Figure 3. Histograms of the dwelling times for (a) 1 mM ATP and (b) 1 mM ATPγS in D_2O and (insets) H_2O. Green lines indicate fits to double-exponential functions used to determine the time constants τ_1 and τ_2 for the events in the dwell.

that represent the temporal behaviors of those processes. The rates were determined by fitting two exponentials to each histogram to express its rise and decay.

For the native substrate in H_2O, the time constants were measured to be on a sub-millisecond time scale (0.4 ± 0.1 and 0.9 ± 0.1 ms), consistent with previous observations.[28,29] As discussed below, the process with the time constant of 0.9 ms is assigned to the hydrolysis reaction. The computationally obtained activation energy is in reasonable agreement with an

estimate of the activation free energy deduced from the experimentally observed time constant for the hydrolysis reaction using the assumption of transition state theory; the computed value is slightly larger than the experimental one by 15.0 kJ/mol (Table 1). The small difference presumably originates from the lack of thermal fluctuations in the computational evaluation of the activation energy. It should be noted, however, that the analysis in the present study compares the activation energies of the ATP substrate with those of chemically identical and similar substrates (i.e., ATP in D_2O and ATPγS in H_2O, respectively). Hence, the modest discrepancies of the absolute activation energies are expected to cancel out and to be insignificant in the present analysis.

The time constants in D_2O were measured to be 0.6 ± 0.1 and 2.7 ± 0.3 ms (Figure 3a), clearly indicating that one of the processes is slowed remarkably. Although the time resolution was not higher than the bin width of 0.5 ms used in the analysis, the time constant of the D_2O-insensitive process (0.6 ms) is close to the shorter one in H_2O (0.4 ms). Thus, the processes with the time constants of 0.4 and 0.9 ms in H_2O likely correspond to those of 0.6 and 2.7 ms in D_2O, respectively. Furthermore, the D_2O-insensitive process represents the P_i release, which does not involve any dissociation of the high-frequency O—H bond leading to a large quantum effect. Hence, the slower processes (0.9 and 2.7 ms in H_2O and D_2O, respectively) are assigned to the hydrolysis reaction. The H_2O/D_2O RRR of 3.0 obtained using the time constants for the hydrolysis reactions in these solvents is in good agreement with the computational prediction of 2.5 (Table 1).

For ATPγS, the time constants were measured to be 1.7 ± 0.2 and 27.2 ± 1.3 ms in H_2O (Figure 3b); again a significant increase of one of the time constants was observed. The process with the longer time constant has already been identified as the hydrolysis reaction.[28,29] The experimental RRR of 30 agrees reasonably well with the computed value of 15 (Table 1).

Figure 4a shows histograms of the experimentally observed catalytic dwelling times for the αArg373Lys mutant as the substrate. As summarized in Table 1, the mutation greatly increases the time constant by 3 orders of magnitude (i.e., RRR = 9.1×10^2 in H_2O solvent and 2.6×10^2 in D_2O solvent), consistent with previous studies.[38,40,41] Interestingly, in contrast to the native protein, the time constant of the mutant was essentially insensitive to the use of D_2O (RRR = 0.88). This rather nontrivial behavior upon mutation was also predicted by the molecular simulations (see the Supporting Information). Figure 4b depicts the energy diagram of the mutant in the TS region. The energy order of the POD and PT processes of the mutant is inverted from that of the native protein. As seen in Table 1, the computed RRRs of the mutants with respect to the native, 1.1×10^3 and 4.0×10^2 in H_2O and D_2O, respectively, and the D_2O-insensitive feature agree well with the experimental observations.

■ DISCUSSION

Reaction Mechanism Predicted by the Molecular Simulations. As shown in Figure 2a, the rate-determining step (RDS) is a proton transfer, PT1, rather than formation of a pentacovalent structure at P_γ during POD, which is often considered to be the RDS. It was also found that POD precedes the rate-determining PT, in contrast to a reaction scheme that has often been assumed in which the lytic water molecule is first activated by PT to a general base in order to form a nucleophile OH$^-$.[8] The sequential order of those events is a
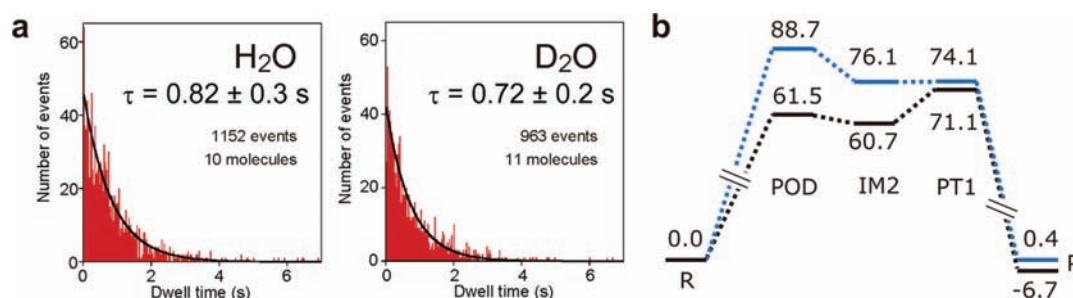
Figure 4. Catalytic ATP hydrolysis activity of the αArg373Lys mutant. (a) Histograms of the dwelling times of the αArg364Lys mutant of thermophilic F_1-ATPase, which corresponds to the αArg373Lys mutant of bovine mitochondrial F_1-ATPase. The bin size of the histograms is 33.3 ms. Black lines indicate fits to single-exponential functions used determine the time constant of the event, τ. (b) Energy diagram (kJ/mol) of the αArg373Lys mutant (blue) compared with that of the native protein (black). ZPE corrections are included in the activation energies of the POD and PT TSs. The energy of PT1 is lower than that of IM2 for the mutant because of a large ZPE for the PT step (see the Supporting Information).

prerequisite for the extremely efficient catalysis of hydrolysis: the reactive $P_\gamma O_3^-$ moiety generated by POD activates the lytic water molecule and greatly reduces the energy barrier of the following PT step in a chain activation manner. In the IM2 intermediate located between the POD and PT processes, the $P_\gamma-O_w$ bond is not completely formed ($P_\gamma-O_w$ bond distance = 1.91 Å; Figure S10 in the Supporting Information). To make a complete $P_\gamma-O_w$ bond for the formation of an inorganic γ-phosphate, a proton of the lytic water molecule must be released. This indicates that the interaction of the lytic water molecule with $P_\gamma O_3^-$ plays a role in stimulating the proton release (i.e., the activation of the lytic water molecule). Other possible reaction schemes were found to be energetically more unfavorable (see the Supporting Information). Stimulation of the POD that triggers the efficient chain activation, and thus is a key mechanism as well, is achieved by strong stabilization of the β-phosphate by the surrounding amino acid groups, as shown below.

The reaction profile of POD suggests that the reaction proceeds in a "dissociative" manner:[42,43] dissociation of the $P_\gamma-O_\beta$ bond is almost completed before the formation of the new P–O bond with the nucleophile. In spite of the dissociative-like TS formation, however, the reaction is not characterized as a conventional S_N1 process. Unlike in other proposed dissociative mechanisms, where a stable intermediate with the γ-metaphosphate detached from the β-phosphate is generated,[13] the metaphosphate intermediate state IM2 is found to be a high-energy quasi-stable state that is separated by very small barriers for the forward and backward steps (Figure 2a), indicating the very transient nature of the $P_\gamma O_3^-$ formation. The potential energy profile therefore well explains the experimental evidence that the formation of a stable and long-lived γ-phosphate is not observed in phosphate transfers from ATP in kinases,[44,45] which disfavor the conventional S_N1 mechanism. The high energy of the metaphosphate intermediate represents its high reactivity, which is capable of greatly reducing the energy barrier of the following rate-determining PT step through strong stabilization by the coupled $P_\gamma-O_w$ bond formation described above. The high-energy intermediate and the small energy barriers from it are characteristics of the chain activation mechanism predicted by the present study. The characteristics are consistent with the previous proposal that the rate-determining PT steps are concerted with POD,[11,16,17] whereas they present a striking contrast to reaction energy profiles of other proposed mechanisms.[8-10,13-15]

Verification of the Reaction Mechanism by Single-Molecule Observations. Single-molecule observation experiments verified the theoretically predicted reaction mechanism, which is characterized by the following three features; (1) the RDS is a PT process; (2) the POD step precedes the PT step; and (3) the metaphosphate intermediate (IM2) and the POD and PT TSs are energetically and geometrically close, with electronic correlation among them.

The first two features were validated by experimental measurements of the hydrolysis reaction rate using D_2O as the solvent and the ATPγS analogue as the substrate, which perturb the PT and POD steps, respectively. As schematically depicted in Figure 5, the reaction profile proposed by the
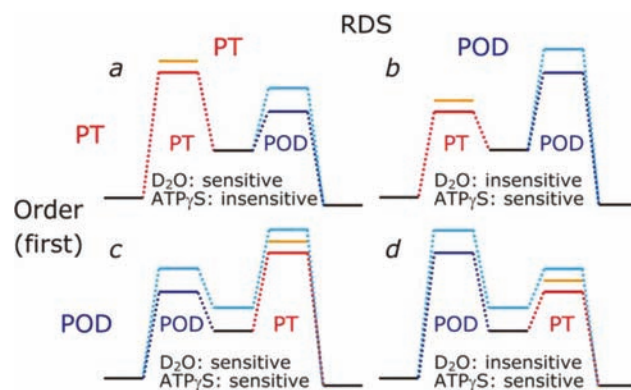

Figure 5. Schematic energy diagrams of possible reaction mechanisms. Energy profiles of the possible reaction paths for the native substrate in H_2O solvent are drawn with black lines for reactant, intermediate, and product states, red lines for PT, and blue lines for POD. Two possibilities each for the RDS and the sequential order produce four possible reaction schemes. Yellow lines at the activation barriers of the PT steps indicate energy increases in D_2O solvent. Energy profiles for ATPγS are represented with cyan lines.

calculation predicts that the reaction rate should decrease when both D_2O solvent and ATPγS substrate are used (case c). D_2O solvent should remarkably reduce the reaction rate if the RDS is PT because of the kinetic isotope effect (KIE) (cases a and c). On the other hand, the hydrolysis reaction should be slowed with ATPγS if the RDS is POD, since POD is affected by the substitution of S for O_γ, which is adjacent to the dissociating P–O bond (cases b and d). Notably, the use of ATPγS should increase the energy of IM2, causing the rate-determining activation barrier for the following PT step to increase as well

even though POD is not the RDS (case *c*). In contrast, the reaction rate should be insensitive to the use of either D_2O as the solvent or $ATP\gamma S$ as the substrate if the two predicted features are not valid, that is, if the RDS is not PT (cases *b* and *d*) and/or PT precedes POD (case *a*); in the latter case, the rate-determining PT step would mask the energy shift for the POD induced by the use of $ATP\gamma S$.

The positive rate sensitivity to the use of both D_2O and $ATP\gamma S$ measured by single-molecule experiments and consistently predicted by the molecular simulations described above (Table 1) clearly validates the remarkable features of the proposed reaction scheme regarding the RDS and the sequential order of the POD and PT steps. The RRR of 3.0 observed by the single-molecule measurements when D_2O was used as the solvent shows that PT forms the TS. It is noteworthy that the KIE of 3.0 is somewhat smaller than that expected for a pure PT reaction, which can be as large as 10. The modest KIE for the PT1 process implies that the proton transfer is coupled with other motions that are insensitive to the H−D substitution. In the present case, as revealed by the QM/MM calculations, the proton transfer in the PT1 process accompanies the bond formation between P_γ and O_w of the lytic water molecule. The modest KIE is therefore a clear indication of the chain activation mechanism underlying the hydrolysis reaction. In contrast, the PT2 process, which does not involve a strong coupling of the PT with other motions, exhibits a larger KIE of 7.4. The success of the prediction of the modest KIE for PT1 demonstrates the high accuracy of the present calculations, which can reproduce the complex coupling in the PT1 process.

The proposed catalytic reaction mechanism was further corroborated with the αArg373Lys mutant, where a catalytic group mainly acting for POD, αArg373 (which corresponds to αArg364 of the thermophilic F_1-ATPase used in the single-molecule experiments; see Methods), is perturbed. The nontrivial disappearance of the KIE indicates that PT is not the RDS in the mutant, which was well-predicted by the molecular simulations (Table 1 and Figure 4): the energy order of the POD and PT processes of the mutant is inverted, and thus, the D_2O-insensitive POD becomes the RDS. The experimentally observed disappearance of the KIE upon mutation indicates a close proximity of the POD and PT activation energies and a strong correlation between those steps, which are characteristics of the chain activation mechanism as described above but can hardly be explained by other proposed mechanisms in which the energies are largely different from each other and the steps are separated by a stable P_i formation or protein conformational changes.[13−15]

Although the unprecedentedly extensive reaction path searches performed in the present study (see the Supporting Information) succeeded in predicting the experimental observations that are crucial for determining the reaction mechanisms, there remains a possibility that a relevant reaction scheme is different yet agrees with the experimental observations. Nevertheless, the computational and experimental findings on the reaction characteristics obtained by the present study provide a solid basis to investigate the biologically fundamental catalytic reactions of NTP hydrolysis.

Molecular Mechanism of the Catalytic Activity and Its Regulation. The reaction profile proposed in the present study together with knowledge obtained previously[16,17] provides clear insights into the molecular mechanisms of the catalytic activity and its regulation. It should be noted that the

chemical−mechanical energy conversion in the motor function requires the latter (i.e., catalytic activity control) coupled with the protein conformational changes in the mechanical motion.

Figure 6 depicts schematically the catalytic mechanism of ATP hydrolysis. First, the catalytic activity can be regulated at
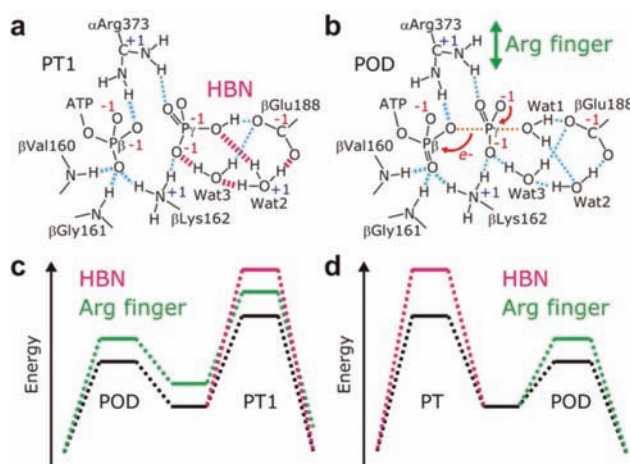

Figure 6. Mechanism of the catalytic activity and its control for chemical−mechanical energy conversion of the motor function proposed on the basis of the reaction energy profile. (a) Formation of the hydrogen-bond network (HBN) that facilitates proton transfers from the lytic water molecule upon its activation. The HBN in the vicinity of the γ-phosphate needs to be arranged properly to allow the PTs, including the RDS, to proceed along the HBN smoothly. (b) Catalysis of the POD process. Upon POD, an electron is transferred from the leaving γ-phosphate moiety to the β-phosphate of ADP. The POD process is therefore catalyzed by hydrogen bonds of the P-loop (βVal160, βGly161, and βLys162) and an Arg finger (αArg373) to the β-phosphate. Especially, movement of the Arg finger coupled to the rotation of the γ subunit can regulate the reactivity of the POD process. (c) Schematic energy diagrams representing changes in the reaction energy profile induced by the HBN formation shown in (a) and the Arg finger shown in (b). Energy diagrams in magenta and green represent those expected for destruction of the HBN and detachment of the Arg finger, respectively. (d) Schematic energy diagrams of a possible reaction process where the sequential order of the processes is opposite to that determined in the present study (i.e., PT precedes POD). The color code of the energy diagrams is the same as that used in (c).

the PT1 process since PT1 is the RDS (Figure 6a). Formation of the hydrogen-bond network of water molecules and polar amino acid groups in the binding pocket that allows efficient PT processes is suggested to be a key mechanism.[12,46] It is noteworthy that no dangling hydrogen bonds of the water molecules are generated during the reaction process after the initial hydrogen-bond network rearrangement (HBR1), which leads to the energetically stable PT processes. Furthermore, a H_3O^+ ion transiently formed in the PT1 process is stabilized by a negatively charged carboxylate of βGlu188,[16,17] which also participates in the hydrogen-bond network. The significant role of βGlu188 in the catalysis is consistent with experimental evidence that removal of the carboxylate of βGlu188 by mutations greatly reduces the ATPase activity.[47−49] A modest reduction of the hydrolysis activity in the αSer344Ala mutant[50] by a factor of 13, the impact of which is comparable to that for a more moderate mutant, βGlu188Asp,[48,49] where the functional carboxylate is preserved, is explained by perturbation of the hydrogen-bond network, since the O−H group of αSer344

forms hydrogen bonds with βArg260 and αAsn341, which also participate in the structural formation of the binding pocket (see the Supporting Information). Mutagenesis studies of the residues in the vicinity of the lytic water molecule (e.g., βGlu188, βArg260, and αSer344) along with theoretical modeling would be interesting in a future study.

The overall reaction barrier height can also be altered by energy control in the POD step, even though POD is not the RDS, as described above (Figure 6c). The sequential order of POD and PT1 revealed by the present study is a crucial factor in enabling the protein to control the enzymatic activity at both steps; if PT were to precede POD (Figure 6d), an energy shift in the POD process would not lead to a change in the reaction rate since the energy change would be masked by the rate-determining PT step.

The catalysis of POD that initiates the chain activation is fulfilled by hydrogen bonds of protein groups of the P-loop (i.e., βVal160, βGly161, and βLys162) and an arginine finger (αArg373) to the β-phosphate of ATP, which accepts an electron upon POD[2,16,17] (Figure 6b). As shown in Figure S16 in the Supporting Information, the hydrogen-bond distances of those groups to the β-phosphate decrease remarkably upon POD, indicating that the hydrogen bonds contribute to stabilization of the POD process. The P-loop and an arginine finger commonly exist in many other NTPases, suggesting that the proposed reaction mechanism is also applicable for those NTPases. For the purpose of the catalytic activity *control*, however, the P-loop groups may not act fully functionally because conformational changes induced at the P-loop could also alter the NTP binding affinity, which must be precisely regulated for the motor function as well. In this regard, therefore, it is suggested that an arginine finger, αArg373, serves as the primary catalyst for the regulation of the enzymatic activity coupled with the motor motion.[17,40,41,51]

CONCLUSIONS

Through a combination of molecular simulation and single-molecule experiment approaches, the present study has provided key electronic and molecular insights into the reaction mechanism of ATP hydrolysis in F_1-ATPase. A kinetic assay identified the RDS and the sequential order of two elementary processes, POD and PT, involved in the hydrolysis and resolved ambiguity in the mechanism due to the multistep nature of the reaction. The proposed chain activation mechanism clearly explains the high catalytic activity of NTPases, which share common NTP binding motifs. The proposed kinetic assay would also be applicable to other NTPase proteins to examine the hydrolysis mechanism. The chemical insight into the enzymatic catalysis of ATP hydrolysis gained in unprecedented detail sheds light on the molecular mechanism of not only the enzymatic activity but also its regulation necessary for the motor function. The combination of molecular simulations and single-molecule observation/manipulation experiments will be a powerful approach for further elucidation of the molecular mechanism of the chemical−mechanical energy conversion in an atomic detail. Such a study combining long-time MD simulations, a recently developed approach for QM/MM free energy calculations,[52] and a single-molecule experimental technique[37] is ongoing.

ASSOCIATED CONTENT

S **Supporting Information**

Supporting descriptions of the methods; detailed information on the reaction profile determined by the QM/MM calculations; hydrogen-bond distances between the triphosphate and the surrounding protein groups; a reaction path without a hydrogen-bond network rearrangement before POD; reaction paths in which PT precedes POD; hydrolysis reaction of ATPγS; and hydrolysis reaction of the αArg373Lys mutant. This material is available free of charge via the Internet at http://pubs.acs.org.

AUTHOR INFORMATION

Corresponding Author
hayashig@kuchem.kyoto-u.ac.jp
Notes
The authors declare no competing financial interest.

ACKNOWLEDGMENTS

REFERENCES

(1) Vale, R. D.; Milligan, R. A. *Science* **2000**, *288*, 88−95.
(2) Weber, J.; Senior, A. E. *Biochim. Biophys. Acta* **1997**, *1319*, 19−58.
(3) Yoshida, M.; Muneyuki, E.; Hisabori, T. *Nat. Rev. Mol. Cell Biol.* **2001**, *2*, 669−677.
(4) Kinosita, K., Jr.; Adachi, K.; Itoh, H. *Annu. Rev. Biophys. Biomol. Struct.* **2004**, *33*, 245−268.
(5) Jones, P. M.; O'Mara, M. L.; George, A. M. *Trends Biochem. Sci.* **2009**, *34*, 520−531.
(6) Sprang, S. R. *Annu. Rev. Biochem.* **1997**, *66*, 639−678.
(7) Wolf-Watz, M.; Thai, V.; Henzler-Wildman, K.; Hadjipavlou, G.; Eizenmesser, E. Z.; Kern, D. *Nat. Struct. Mol. Biol.* **2004**, *11*, 945−949.
(8) Schweins, T.; Langen, R.; Warshel, A. *Nat. Struct. Mol. Biol.* **1994**, *1*, 476−484.
(9) Štrajbl, M.; Shurki, A.; Warshel, A. *Proc. Natl. Acad. Sci. U.S.A.* **2003**, *100*, 14834−14839.
(10) Klähn, M.; Rosta, E.; Warshel, A. *J. Am. Chem. Soc.* **2006**, *128*, 15310−15323.
(11) Li, G.; Cui, Q. *J. Phys. Chem. B* **2004**, *108*, 3342−3357.
(12) Yang, Y.; Yu, H.; Cui, Q. *J. Mol. Biol.* **2008**, *381*, 1407−1420.
(13) Grigorenko, B. L.; Nemukhin, A. V.; Shadrina, M. S.; Topol, I. A.; Burt, S. K. *Proteins: Struct., Funct., Bioinf.* **2007**, *66*, 456−466.
(14) Grigorenko, B. L.; Rogov, A. V.; Topol, I. A.; Burt, S. K.; Martinez, H. M.; Nemukhin, A. V. *Proc. Natl. Acad. Sci. U.S.A.* **2007**, *104*, 7057−7061.
(15) Beke-Somfai, T.; Lincoln, P.; Nordén, B. *Proc. Natl. Acad. Sci. U.S.A.* **2011**, *108*, 4828−4833.
(16) Dittrich, M.; Hayashi, S.; Schulten, K. *Biophys. J.* **2003**, *85*, 2253−2266.
(17) Dittrich, M.; Hayashi, S.; Schulten, K. *Biophys. J.* **2004**, *87*, 2954−2967.
(18) Nakamoto, R. K.; Ketchum, C. J.; Al-Shawi, M. K. *Annu. Rev. Biophys. Biomol. Struct.* **1999**, *28*, 205−234.
(19) Gao, Y. Q.; Yang, W.; Karplus, M. *Cell* **2005**, *123*, 195−205.
(20) Junge, W.; Sielaff, H.; Engelbrecht, S. *Nature* **2009**, *259*, 364−370.

(21) Noji, H.; Yasuda, R.; Yoshida, M.; Kinosita, K., Jr. *Nature* **1997**, *386*, 299−302.

(22) Yasuda, R.; Noji, H.; Yoshida, M.; Kinosita, K., Jr.; Itoh, H. *Nature* **2001**, *410*, 898−904.

(23) Sambongi, Y.; Iko, I.; Tanabe, M.; Omote, H.; Iwamoto-Kihara, A.; Ueda, I.; Yanagida, T.; Wada, Y.; Futai, M. *Science* **1999**, *286*, 1722−1724.

(24) Diez, M.; Zimmermann, B.; Börsch, M.; Körig, M.; Schweinberger, E.; Steigmiller, S.; Reuter, R.; Felekyan, S.; Kudryavtsev, V.; Seidel, C. A. M.; Gräber, P. *Nat. Struct. Mol. Biol.* **2004**, *11*, 135−141.

(25) Spetzler, D.; York, J.; Daniel, D.; Fromme, R.; Lowry, D.; Frasch, W. *Biochemistry* **2006**, *45*, 3117−3124.

(26) Shimabukuro, K.; Yasuda, R.; Muneyuki, E.; Hara, K. Y.; Kinosita, K., Jr.; Yoshida, M. *Proc. Natl. Acad. Sci. U.S.A.* **2003**, *100*, 14731−14736.

(27) Ariga, T.; Muneyuki, E.; Yoshida, M. *Nat. Struct. Mol. Biol.* **2007**, *14*, 841−486.

(28) Adachi, K.; Oiwa, K; Nishizaka, T.; Furuike, S.; Noji, H.; Itoh, H.; Yoshida, M.; Kinosita, K., Jr. *Cell* **2007**, *130*, 309−321.

(29) Watanabe, R.; Iino, R.; Noji, H. *Nat. Chem. Biol.* **2010**, *6*, 814−820.

(30) Ueno, H.; Nishikawa, S.; Iino, R.; Tabata, K. V.; Sakakihara, S.; Yanagida, T.; Noji, H. *Biophys. J.* **2010**, *98*, 2014−2023.

(31) Bowler, M. W.; Montgomery, M. G.; Leslie, A. G. W.; Walker, J. E. *J. Biol. Chem.* **2007**, *282*, 14238−14242.

(32) Masaike, T.; Koyama-Horibe, F.; Oiwa, K.; Yoshida, M.; Nishizaka, T. *Nat. Struct. Mol. Biol.* **2008**, *15*, 1326−1333.

(33) Okuno, D.; Fujisawa, R.; Iino, R.; Hirono-Hara, Y.; Imamura, H.; Noji, H. *Proc. Natl. Acad. Sci. U.S.A.* **2008**, *105*, 20722−20727.

(34) Ikeguchi, M. *J. Comput. Chem.* **2004**, *25*, 529−541.

(35) Hayashi, S.; Ohmine, I. *J. Phys. Chem. B* **2000**, *104*, 10678−10691.

(36) Schmidt, M. W.; Baldridge, K. K.; Boatz, J. A.; Elbert, S. T.; Gordon, M. S.; Jensen, J. H.; Koseki, S.; Matsunaga, N.; Nguyen, K. A.; Su, S.; Windus, T. L.; Dupuis, M.; Montgomery, J. A., Jr. *J. Comput. Chem.* **1993**, *14*, 1347−1363.

(37) Watanabe, R.; Okuno, D.; Sakakihara, S.; Shimabukuro, K.; Iino, R.; Yoshida, M.; Noji, H. *Nat. Chem. Biol.* **2012**, *8*, 86−92.

(38) Komoriya, Y.; Ariga, T.; Iino, R.; Imamura, H.; Okuno, D.; Noji, H. *J. Biol. Chem.* **2012**, *287*, 15134−15142.

(39) Yasuda, R.; Noji, H.; Kinosita, K., Jr.; Yoshida, M. *Cell* **1998**, *93*, 1117−1124.

(40) Soga, S.; Noumi, T.; Takeyama, M.; Maeda, M.; Futai, M. *Arch. Biochem. Biophys.* **1989**, *268*, 643−648.

(41) Turina, P.; Aggeler, R.; Lee, R. S. F.; Senior, A. E.; Capaldi, R. A. *J. Biol. Chem.* **1993**, *268*, 6978−6984.

(42) Maegley, K. A.; Admiraal, S. J.; Herschlag, D. *Proc. Natl. Acad. Sci. U.S.A.* **1996**, *93*, 8160−8166.

(43) Du, X.; Black, G. E.; Lecchi, P.; Abramson, F. P.; Sprang, S. R. *Proc. Natl. Acad. Sci. U.S.A.* **2004**, *101*, 8858−8863.

(44) Lowe, G.; Sproat, B. S. *J. Biol. Chem.* **1980**, *255*, 3944−3951.

(45) Hassett, A.; Blätter, W.; Knowles, J. R. *Biochemistry* **1982**, *21*, 6335−6340.

(46) Ohnishi, H.; Mochizuki, N.; Morales, M. F. *Biochemistry* **2004**, *43*, 3757−3763.

(47) Senior, A. E.; Al-Shawi, M. K. *J. Biol. Chem.* **1992**, *267*, 21471−21478.

(48) Park, M.-Y.; Omote, H.; Maeda, M.; Futai, M. *J. Biochem.* **1994**, *116*, 1139−1145.

(49) Amano, T.; Tozawa, K.; Yoshida, M.; Murakami, H. *FEBS Lett.* **1994**, *348*, 93−98.

(50) Li, W.; Brudecki, L. E.; Senior, A. E.; Ahmad, Z. *J. Biol. Chem.* **2009**, *284*, 10747−10754.

(51) Abrahams, J. P.; Leslie, A. G. W.; Lutter, R.; Walker, J. E. *Nature* **1994**, *370*, 621−628.

(52) Kosugi, T.; Hayashi, S. *J. Chem. Theory Comput.* **2012**, *8*, 322−334.